J. Fluid Mech. (2025), *vol.* 1007, A9, doi:10.1017/jfm.2024.1109

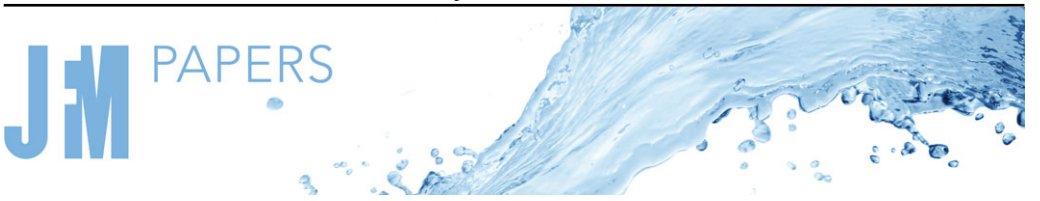

Influence of depth-ratio on turbulence transition in the wake of wall-mounted prisms

Shubham Goswami[1] **and Arman Hemmati**[1]

[1]Department of Mechanical Engineering, University of Alberta, Edmonton, AB T6G 2R3, Canada

Corresponding author: Arman Hemmati, arman.hemmati@ualberta.ca

(Received 6 June 2024; revised 14 November 2024; accepted 18 November 2024)

This paper presents a numerical investigation of the turbulence transition phenomenon in the wake of wall-mounted prisms. Large-eddy simulations are performed at $Re = 1 \times 10^3 - 5 \times 10^3$ for prisms with a range of aspect ratio (height to width) from 0.25 to 1.5, and depth ratios (length to width) between 1 and 4. The results show that the wake irregularity is enhanced with increasing depth ratio, evidenced by higher turbulent kinetic energy (≈90 %) near the leading edge, and the onset of irregular, unsteady vortex shedding. This is attributed to interactions between Kelvin–Helmholtz instability (KHI) of the shear layer and large-scale vortex shedding, and it is induced by an unsteady shear layer, resembling flapping-like motion. These interactions elevate the flow momentum due to increased turbulence intensity and mixing, contributing to the wake transition phenomenon. To this end, this study defines the role of depth ratio in the transition phenomenon by showing that increasing depth ratio (e.g. from 1 to 4) leads to earlier onset of KHIs in the shear layer. These instabilities intensify with depth ratio, resulting in stronger interactions between shear layer and large-scale vortex shedding. Specifically, KHI-induced vortices interact more frequently with large-scale wake structures for higher depth ratio prisms, exciting larger flow fluctuations and irregular wake patterns. This interaction alters the frequency and coherence of vortex shedding, revealing a complex coupling mechanism that drives the transition to turbulence.

Key words: wakes, separated flows, vortex dynamics

1. Introduction

Separated flows over sharp-edged, wall-mounted bluff bodies, such as prisms, has garnered increasing attention due to their relevance in various industrial applications (Goswami

& Hemmati 2020, 2021*a*,*b*). These flows are complex and multifaceted, owing to their inherent three-dimensional nature, and are primarily attributed to end effects (Wang & Zhou 2009). As the oncoming flow encounters the leading edge, it decelerates and forms a boundary layer along the prism surfaces. This boundary layer subsequently separates, creating a highly disturbed region of flow known as the wake (Zdravkovich 1997). One prominent feature of the wake is the formation of large-scale coherent structures, which contain a significant portion of the total fluctuating energy, thus playing a vital role in momentum transfer and mixing processes. The formation of these structures strongly depends on the state of the wake, which can be laminar, transitional or turbulent. Transition can occur in three key regions, commonly observed in various geometries, including both circular and rectangular cylinders: (i) within the wake, (ii) in the free-shear layers, and (iii) within the boundary layer (Zdravkovich 1997). In the context of sharp-edged bluff body wake, such as a wall-mounted prism, transition to turbulence occurs rapidly in the free shear layers, with the wake becoming fully turbulent due to flow separation at the leading edges (Martinuzzi 2008). Moreover, transition to turbulence is influenced by both Reynolds number ($Re = U_b d/\nu$, where d is the width of the prism in the spanwise direction) and geometrical features of the flow, including depth ratio ($DR = l/d$, where l is the length of the prism in the streamwise direction), aspect ratio ($AR = h/d$, where h is the height of the prism in flow normal direction), and free-end effects, particularly in the case of wall-mounted prisms (Zdravkovich 1997).

At elevated Reynolds numbers ($Re > 10^3$), it is well documented that separated shear layers have the capacity to reattach over the side and top surfaces of the prism, provided that there is a significant increase in depth ratio (Rastan *et al.* 2021). Further, increasing depth ratio entails enhancement of the downwash flow, which suppresses the wake unsteadiness (Goswami & Hemmati 2022). Meanwhile, aspect ratio plays a role in intensifying the upwash flow and contributing to the overall wake unsteadiness (Saha 2013). Thus enhancement of the unsteadiness in the wake of wall-mounted prisms can be achieved by either increasing the prism aspect ratio or reducing its depth ratio. This heightened wake unsteadiness suggests that such abrupt changes in geometry may be associated with the transition to turbulence.

Goswami & Hemmati (2022) studied the wake of small aspect ratio wall-mounted prisms with increasing depth ratio at low Reynolds numbers, and observed the suppression of spatio-temporal features with depth ratio. Previously, Rastan *et al.* (2021) made similar observations at Reynolds number $Re = 1.2 \times 10^4$, which is within the moderate range of Reynolds numbers ($10^3 \ll Re \ll 10^4$). They demonstrated that increasing the prism depth ratio led to diminished vortex shedding, which was attributed to the suppressed interactions between the separating shear layer and the wake. This suppression was linked to strengthening of the downwash flow. Zargar *et al.* (2022) further demonstrated that increasing the Reynolds number above 750 for a large-depth-ratio prism ($DR = 5$) leads to an irregular (unstable) unsteady regime resembling a transitional state. The irregular shedding resulted in flow reattachment and subsequent detachment from the prism surfaces. The majority of studies on wall-mounted prisms have focused on low ($10^2 \leqslant Re \leqslant 10^3$) and high ($Re \geqslant 10^4$) Reynolds number ranges, with limited attention given to the moderate range of Reynolds numbers. The moderate Reynolds number range ($10^3 \leqslant Re \leqslant 10^4$) is associated with the onset of complex flow phenomena for wall-mounted long prisms (Zargar *et al.* 2022), including transition to turbulence in the wake, which significantly influences the wake dynamics and aerodynamic forces. Understanding these phenomena is crucial for applications involving wall-mounted prisms, as they can significantly influence the wake dynamics and consequently the aerodynamic forces and structural response

Parameter	Range	Increments
Depth ratio ($DR = l/d$)	1−4	1
Aspect ratio ($AR = h/d$)	0.25−1.5	0.25
Reynolds number ($Re = U_b d/\nu$)	1×10^3−5×10^3	0.5×10^3

Table 1. Parametric space of the study.

(Martinuzzi 2008; Hemmati *et al.* 2016; Zargar *et al.* 2022). As such, it is important to investigate and characterize the wake of wall-mounted prisms in this regime.

Previously, the influence of depth ratio on global unsteadiness and interactions between Kelvin–Helmholtz instability (KHI) and large-scale vortex shedding have been reported for infinite-span suspended prisms (Zhang *et al.* 2023). However, these interactions differ significantly compared to the case of wall-mounted prisms, due mainly to the infinite-span nature of the prisms, where the wake is bounded by free-end effects (Wang & Zhou 2009). Thus in the context of wall-mounted prisms, interactions between KHI and large-scale vortex shedding, influenced by depth ratio and free-end effects, have not been quantified in the past literature. The current study investigates the role of depth ratio in turbulence transition at $10^3 \leqslant Re \leqslant 10^4$. Specifically, this study investigates the possibility of enhanced momentum transport with increasing depth ratio as a precursor to wake transition. We hypothesize that an unsteady shear layer may enhance interactions between leading-edge shear layer instabilities and prism surfaces, particularly at large depth ratios. This enhanced interaction could elevate flow momentum and potentially contribute to the transition phenomenon.

Numerical investigations are performed at Reynolds numbers 1×10^3−5×10^3 for wall-mounted prisms with aspect ratios 0.25−1.5 and a range of depth ratios (1−4). For brevity, we focus our main analysis on the case $Re = 2.5 \times 10^3$, $AR = 1$ and $DR = 1$ and 4, which avails investigation of the wake at extreme geometrical settings. Observations and insights from these specific cases are then expanded across the broad parameter space considered in this study and presented later on. The results are discussed in the context of the unsteady shear layer, wake frequency signatures, and enhanced interactions using the Poisson equation. Finally, the triadic interactions are quantified using bi-spectral mode decomposition to further understand the transition phenomenon. This paper is structured as follows. Section 2 presents the problem description, followed by the results in § 3. Finally, the conclusions are presented in § 4.

2. Problem description

Large-eddy simulations (LES) with the dynamic Smagorinsky sub-grid scale model (Durbin & Reif 2011) within OpenFOAM were utilized to study the wake. The computational domain consisted of a rectangular prism with aspect ratios $AR = h/d = 0.25, 0.5, 1, 1.5$ and depth ratios $DR = l/d = 1, 2, 3, 4$ mounted on the base of the domain with dimensions $L_u = 10d$, $L_d = 20d$, $H = 6d$ and $W = 12d$. Numerical simulations were performed at Reynolds numbers $Re = U_b d/\nu = 1 \times 10^3$−$5 \times 10^3$, with increments of 0.5×10^3, where U_b is the bulk velocity, d is the width of the prism, and ν is the kinematic viscosity. The parametric space of the study is presented in table 1. A non-homogeneous structured grid consisting of 25×10^6 and 40×10^6 elements, depending on the depth ratio, was developed for this study. Domain and grid for the case $DR = 4$ are

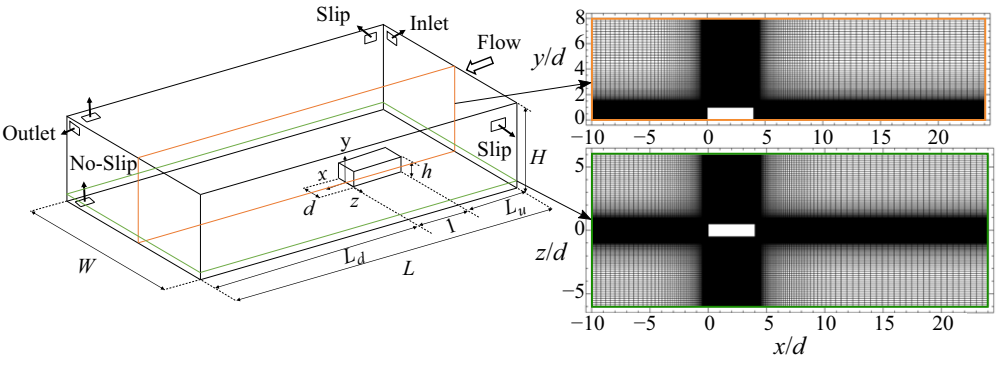

Figure 1. Computational domain (not to scale) and spatial grid distribution for the wall-mounted thin prism with $DR = 4$, presented in top view at $y/d = 0.5$ (top) and side view at $z/d = 0$ (bottom).

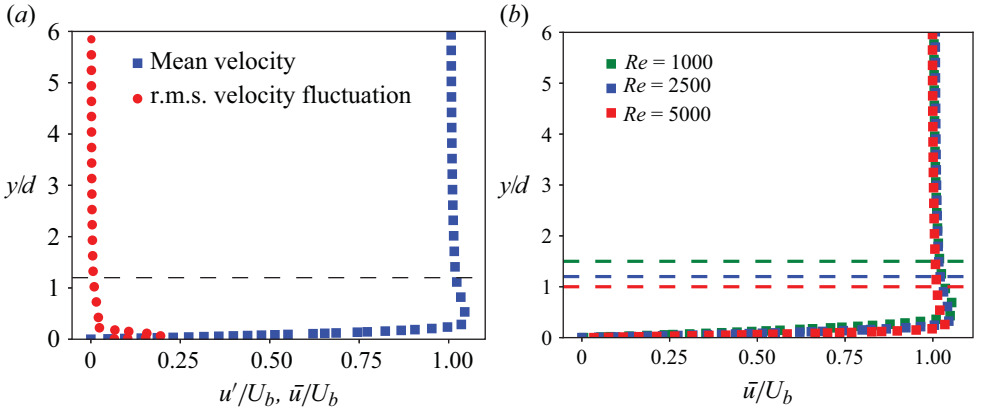

Figure 2. (*a*) Distribution of the time-averaged values and root mean square (r.m.s.) of the streamwise velocity ($\overline{u}$ and u') at the location of the leading edge of the prism at $Re = 2.5 \times 10^3$. (*b*) Distribution of the time-averaged streamwise velocity ($\overline{u}$) at the location of the leading edge of the prism at $Re = 1 \times 10^3$, 2.5×10^3, 5×10^3. Measurements were performed in the absence of the prism. The dashed line shows the boundary layer thickness (δ/d).

presented in figure 1. The inlet boundary conditions were set to uniform flow ($u = U_b$, $v = w = 0$), with an outflow boundary condition ($\partial u/\partial n = \partial p/\partial n = 0$) applied at the outlet. Ceiling and lateral boundaries were modelled as free-slip, while a no-slip wall condition was imposed on the ground and the prism. This computational set-up closely resembled that of Goswami & Hemmati (2022, 2023). The natural boundary layer thickness (δ) varied between $\delta/d \approx 1.5$ and $\delta/d \approx 1$ for $Re = 1 \times 10^3$ and 5×10^3, respectively, when simulating the flow without placing the prism in the domain. Boundary layer thickness was determined as the distance from the wall to the location where the streamwise mean velocity reaches 99 % of the free-stream velocity. As an example, the boundary-layer thickness at $Re = 2.5 \times 10^3$ was $\delta/d \approx 1.2$, as shown in figure 2(*a*). Since the boundary layer thickness changes with Reynolds number (see figure 2*b*), implications of boundary layer thickness and dynamics on the wake topology is naturally incorporated in the current analysis. As noted by Behera & Saha (2019), the implications of boundary layer thickness on the wake are negligible considering a small (~ 10 %) variation in δ.

Study	N_{total}	Domain size	y^+_{max}	$\overline{C_d}$	$\lvert\Delta\overline{C_d}\,\%\rvert$	$\overline{C_l}$	$\lvert\Delta\overline{C_l}\,\%\rvert$	C'_d	C'_l	C'_s
Domain 1	17.3×10^6	$30d \times 5d \times 10d$	0.8	1.102	5.60	0.921	5.14	0.016	0.039	0
Domain 2	19.6×10^6	$30d \times 6d \times 12d$	0.8	1.041	–	0.875	–	0.012	0.032	0
Domain 3	20.9×10^6	$35d \times 6d \times 12d$	0.8	1.043	0.19	0.876	0.10	0.012	0.032	0
Grid 1	5.1×10^6	$30d \times 6d \times 12d$	3.1	1.100	5.51	0.914	5.33	0.018	0.041	0
Grid 2	15.1×10^6	$30d \times 6d \times 12d$	1.55	1.061	2.36	0.899	3.55	0.013	0.033	0
Grid 3	19.6×10^6	$30d \times 6d \times 12d$	0.8	1.041	0.38	0.875	0.90	0.012	0.032	0
Grid 4	25.2×10^6	$30d \times 6d \times 12d$	0.44	1.037	–	0.868	–	0.012	0.032	0

Table 2. Domain and grid sensitivity analysis results for wall mounted prism with $DR = 4$ at $Re = 2.5 \times 10^3$. The relative error is calculated with respect to domain 2 and grid 4, respectively.

In the current study, the change in δ is $\sim 8\,\%$. A thick boundary layer ($\delta/h \geqslant 1$, fully submerged body) is considered in the current study, which means that the oncoming flow over the prism length plays a significant role in dictating the wake characteristics through variations in the strength of the separated vortex sheet over the prism length (Bourgeois *et al.* 2011).

Second-order implicit backward Euler numerical schemes were used for temporal discretization, and the diffusive and convective fluxes were approximated using central difference schemes. The discretized equations were then solved using a pressure implicit with splitting operator (PISO) algorithm (Goswami & Hemmati 2024). Time-marching simulations were performed by adjusting the temporal grid to maintain a maximum Courant number below 0.8. Moreover, the time step size ($\Delta t^* = \Delta t\, U_b/d = 0.001$) was selected such that the ratio of eddy turnover time (τ_η) to Δt for the smallest dissipative eddy (Pope 2001) yields at least 50 time steps. All simulations continued for 150 vortex shedding cycles, while the last 100 cycles were used for post-processing. This duration ensured that transient effects from the initial conditions had dissipated (Hemmati *et al.* 2018). The sampling frequency of data used for spectral analysis was $f^*_s \approx 500$, based on the simulation time step, such that data were collected every time step. Simulations were completed on a Digital Research Alliance of Canada computing cluster, utilizing 256 Intel $E5{-}2683$ v4 Broadwell cores with 125 GB of shared memory, requiring 6×10^5 core hours in total.

2.1. *Verification and validation*

Numerical simulations were verified by evaluating the sensitivity of results to domain size and grid resolution. To start, we acknowledge that the present computational domain was designed larger than those employed in previous studies (Saha 2013; Rastan *et al.* 2021). The set-up, domain and grid configuration were adopted from Goswami & Hemmati (2022, 2023). Blockage ratio (β) and domain height (H) were set as 0.01 and $6d$, respectively. These criterion followed the practices of Sohankar *et al.* (1998) and Saha (2013), which suggested $\beta = (d \times h)/(W \times H) \leqslant 0.05$ and $H \geqslant h + 5d$, to ensure negligible effects of domain on the global flow features. Comparison of mean drag ($\overline{C_d}$) and lift ($\overline{C_l}$) coefficients in table 2 indicated a negligible influence of the domain size, with domain 2 ($30d \times 6d \times 12d$) being sufficient to capture the flow features of interest. Moreover, the root mean square (r.m.s.) of drag, lift and side force obtained from domains 2 and 3 are in close agreement. Domain sensitivity was further investigated in figure 3 by comparing mean and turbulent flow profiles at $x/d = 1$ downstream of the prism. The results in figure 3 further suggests a close agreement between domains 2 and 3, while the

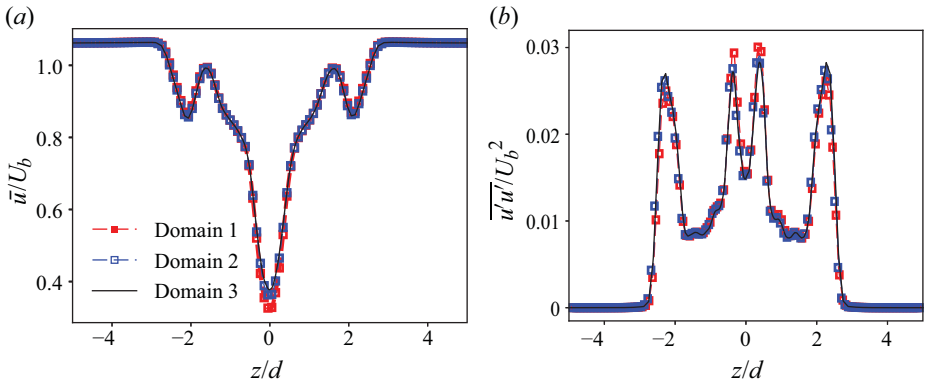

Figure 3. Effect of domain size on mean and turbulent wake characteristics at $x/d = 1$ and $y/d = 1$ for prism with $DR = 4$ at $Re = 2.5 \times 10^3$. Shown are (*a*) $\overline{u}$ and (*b*) $\overline{u'u'}$.

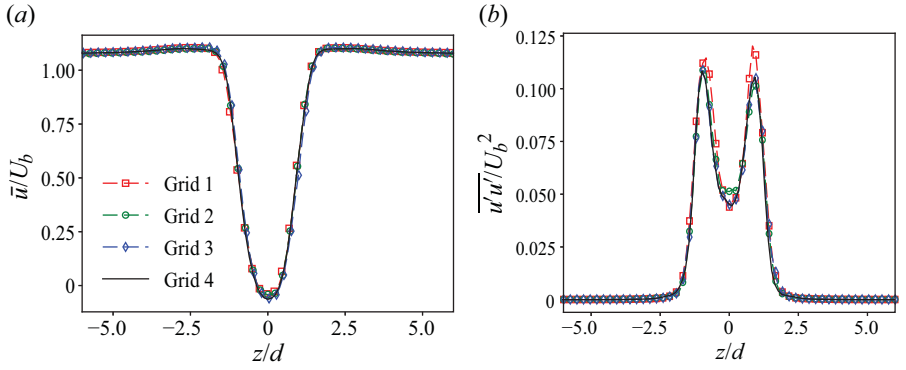

Figure 4. Effect of grid size on mean and turbulent wake characteristics at $x/d = 2$ and $y/d = 0.5$ for prism with $DR = 4$ at $Re = 2.5 \times 10^3$. Shown are (*a*) $\overline{u}$ and (*b*) $\overline{u'u'}$.

influnce of blockage is apparent in domain 1. As such, domain 2 is selected for the present study.

Grid sensitivity was assessed using four grids that were successively refined to include 5.1×10^6, 15.1×10^6, 19.6×10^6 and 25.2×10^6 elements. Relative errors in the mean drag ($\overline{C_d}$) and lift ($\overline{C_l}$) between grids 3 and 4 were below 1 %, indicating grid convergence for grid 3 (details in table 2). Furthermore, the r.m.s. values of drag, lift and side force obtained from grids 3 and 4 are in close agreement. A maximum deviation ~ 0.1 % was noted for the r.m.s. of lift, while the side force coefficient remained constant at $C_s' = 0$ for all grids and domains. The side force coefficient is expected to be zero for the current set-up due to the symmetric nature of the time-averaged flow around the prism in the lateral direction. Here, drag and lift coefficients relate to mean axial ($\overline{F}_x$) and normal ($\overline{F}_y$) forces, respectively. Further, the sensitivities of mean and turbulent flow to changing grid sizes are examined in figure 4 by comparing their profiles at $x/d = 2$ downstream of the prism. Only one axial location is presented for brevity. Comparisons in figure 4 showed excellent agreement with < 1 % deviation between grids 3 and 4. This suggests that the grid resolution for grid 3 is sufficient to capture the flow features of interest.

The present study necessitates accurate resolution of the smallest resolvable flow features, such as the leading-edge shear layer and the wake structures in the immediate

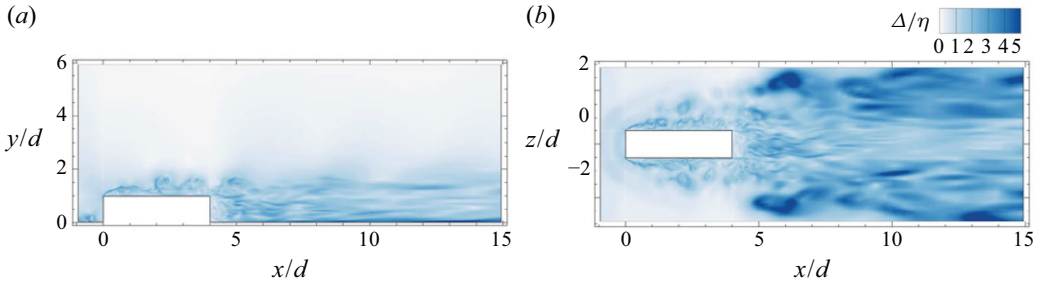

Figure 5. Contours of the ratio of grid size to Kolmogorov length scale (Δ/η) at (*a*) $z/d = 0$ and (*b*) $y/d = 0.5$, for the case $DR = 4$ at $Re = 2.5 \times 10^3$.

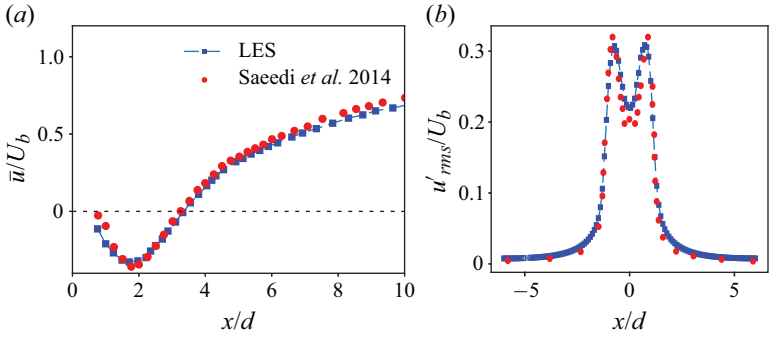

Figure 6. Comparison of (*a*) mean axial velocity ($\overline{u}$) and (*b*) r.m.s. velocity (u'_{rms}) profiles obtained from LES with the experimental results of Saeedi *et al.* (2014).

vicinity of the prism. To this end, the grid size should be comparable to the Kolmogorov length scale (Moin & Mahesh 1998). Therefore, we investigate the ratio of grid size (Δ) to Kolmogorov length scale (η) for further verification. Kolmogorov length scale is defined as $\eta = (\nu^3/\epsilon)^{1/4}$, where ν is the kinematic viscosity, $\epsilon = 2\nu(s'_{ij}s'_{ij})$ is the turbulent energy dissipation rate, and s'_{ij} is the strain-rate tensor given as $s'_{ij} = \frac{1}{2}(\partial u'_j/\partial x_i + \partial u'_i/\partial x_j)$ (Pope 2001). The grid size is calculated as $\Delta = \sqrt[3]{\Delta x \times \Delta y \times \Delta z}$. Using direct numerical simulations, Yakhot *et al.* (2006) and Saeedi *et al.* (2014) suggested $\Delta/\eta = 2{-}5$ in the critical regions of the wake of wall-mounted prisms. Additionally, Celik *et al.* (2009) and Rastan *et al.* (2021) recommended $20 \leqslant \Delta/\eta \leqslant 40$ for LES. Contours of Δ/η are presented in figure 5 on both the normal ($y/d = 0.5$) and spanwise ($z/d = 0$) planes for the prism with $DR = 4$. The results demonstrate that maximum Δ/η is ~ 5 at $x/d = 15$, with Δ/η between 1 and 3 in the immediate vicinity of the prism. This indicates that the resolution of grid 3 is sufficient to capture the critical flow features.

Due to a lack of existing experimental data for our specific case (prism with $DR = 4$, $Re = 2.5 \times 10^3$), we adopted an alternate validation approach. We mimicked the set-up of Saeedi *et al.* (2014) for an $AR = 4$ prism at $Re = 1.2 \times 10^5$ using LES. The LES grid resolution and computational set-up mirrored the present study. Mean axial velocity profiles from the LES agreed well with Saeedi *et al.* (2014), such that we had less than 5 % deviation (figure 6*a*). Figure 6(*b*) further shows satisfactory agreement between LES and experimental results in capturing the r.m.s. velocity profiles. The trends at the peak and into the wake are well reproduced by the numerical simulations. This outcome validated our numerical set-up.

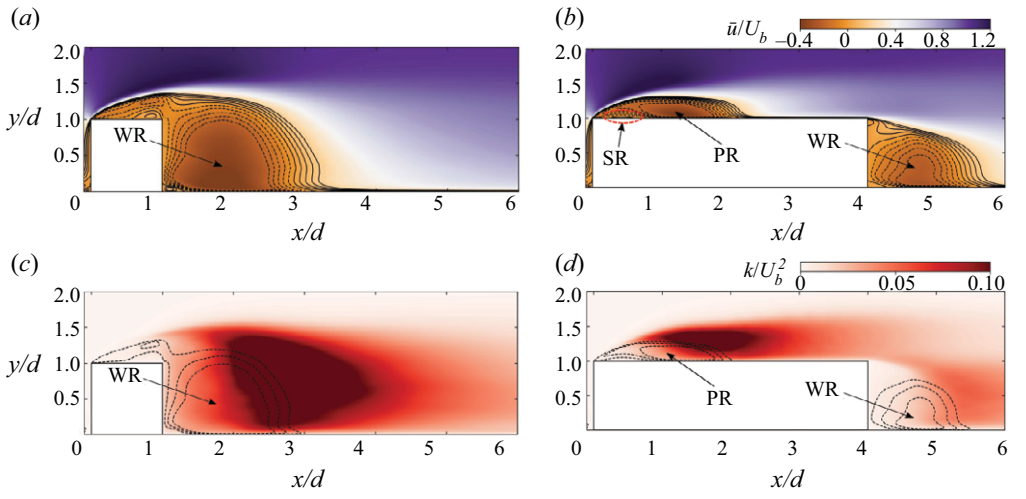

Figure 7. (*a*,*b*) Mean streamwise velocity ($\overline{u}$) and (*c*,*d*) turbulent kinetic energy (k) contours overlaid with mean velocity streamlines for (*a*,*c*) $DR = 1$ and (*b*,*d*) $DR = 4$ prisms.

3. Results and discussion

We begin by reporting the main features of the mean flow. As shown in figures 7(*a*) and 7(*b*), streamlines highlight the presence of flow separation at the leading edge, which in case $DR = 1$ prolongs into the wake and reattaches at $x/d \approx 2.12$ for $DR = 4$. Reattachment length is quantified by tracing the time-averaged wall shear stress across the top surface of the $DR = 4$ prism. A large-scale recirculation region is present on the top surface of $DR = 4$, hereby referred to as the primary recirculation (PR) region. A second recirculation bubble is present below the PR region, noted as the secondary recirculation (SR) zone. Indeed, the reverse flow induced in the near-wall region of the PR forms a boundary layer moving upstream, resulting in the formation of the SR. Following the trailing-edge separation of the flow, a tertiary recirculation region is formed, referred to as the wake recirculation (WR) region. For a short prism, the absence of PR and SR is attributed to a lack of flow reattachment on the prism surfaces. As such, only WR is noted due to shedding of the leading-edge shear layer directly into the wake. Contours of turbulent kinetic energy ($k = (u_i' u_i')/2$) are presented in figures 7(*c*) and 7(*d*). Initially, both prisms highlight an almost laminar state of the leading-edge shear layer. Instabilities associated with the leading-edge shear layer amplify the intensity of fluctuating velocities, initiating the transition to turbulence (Wang & Zhou 2009). These regions of intense fluctuations result in high turbulence intensity (u_i'), thus maximizing k. For the larger prisms, maximum k occurs on the prism top surface, while the shorter prisms experience it in the wake. The region of maximum k occurs in the primary vortex shedding region.

Qualitative illustrations of instantaneous vortex structures for $DR = 1$ and 4 are presented in figure 8. Following the leading-edge separation, the shear layer undergoes distinct stages of growth and primary instability formation (Moore *et al.* 2019*a*). This triggers the formation of a KHI of the shear layer for both prisms, as evidenced by the finite spanwise vortex rollers forming near the leading edge. Such rollers are delayed and less frequent for $DR = 1$, and their formation occurs over a larger distance compared to $DR = 4$. This is evident from the distrubution of maximum turbulent kinetic energy (k_{max}) along the mid-span ($z/d = 0$) of both prisms at $Re = 2.5 \times 10^3$ in figure 9. Previous studies (Moore *et al.* 2019*b*) have used similar methods to identify the location of vortex

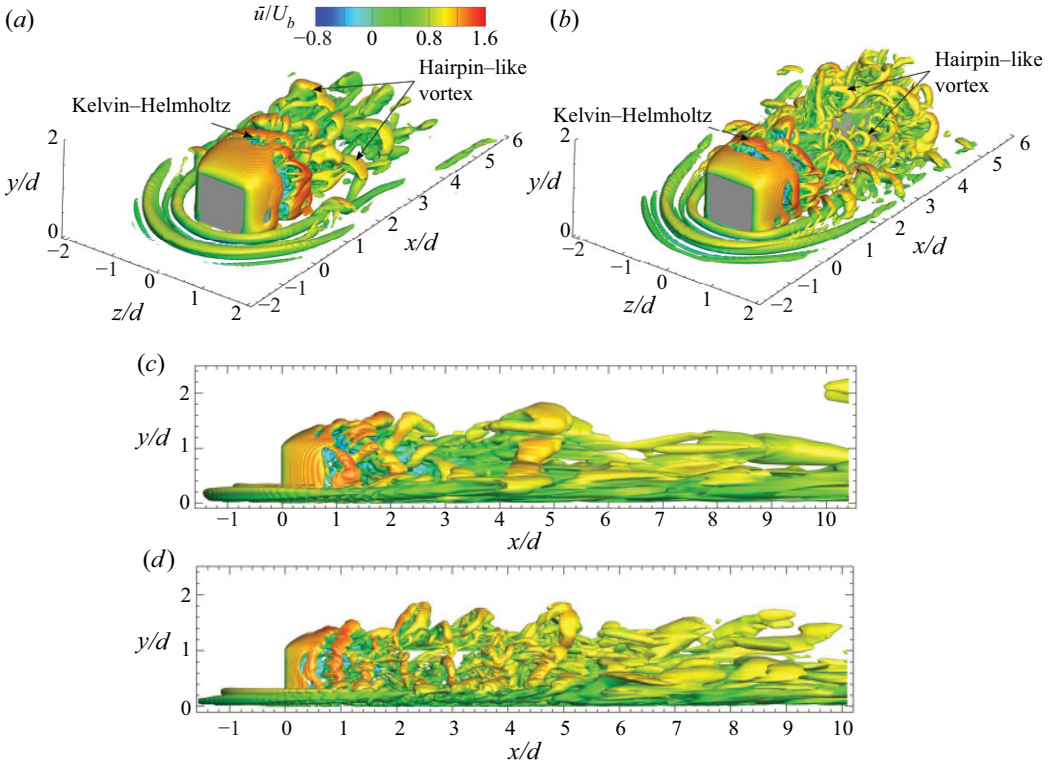

Figure 8. Instantaneous vortex structures overlaid with axial velocity (u) contours for (a) $DR = 1$ and (b) $DR = 4$ prisms identified using the Q-criterion ($Q^* = 1$). Lateral view of the instantaneous vortex structures for (c) $DR = 1$ and (d) $DR = 4$ prisms.

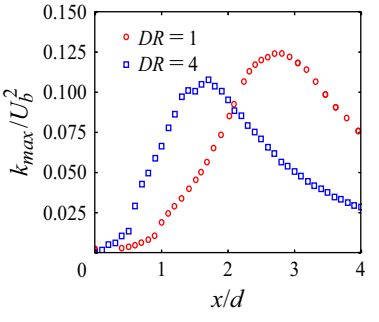

Figure 9. Distribution of maximum turbulent kinetic energy (k_{max}) along the mid-span ($z/d = 0$) of both prisms at $Re = 2.5 \times 10^3$.

roll-up behind sharp-edged bluff bodies. Figure 9 shows that the roll-up phenomenon, i.e. the location of maximum turbulent kinetic energy, is delayed for $DR = 1$ compared to $DR = 4$. In case $DR = 4$, the roll-up occurs close to $x/d \approx 2$, while it occurs at $x/d \approx 3$ for $DR = 1$. These rollers become more prominent with increasing depth ratio. Thus there is evidence of a strong dependence on depth ratio for the generation of these instabilities. Evidence of the flow periodicity and frequency signatures is provided in § 3.2. Figures 8(c) and 8(d) presents the lateral view of the instantaneous vortex structures for $DR = 1$ and 4 prisms. In case $DR = 1$, amplified quasi-periodic perturbations resulting from an

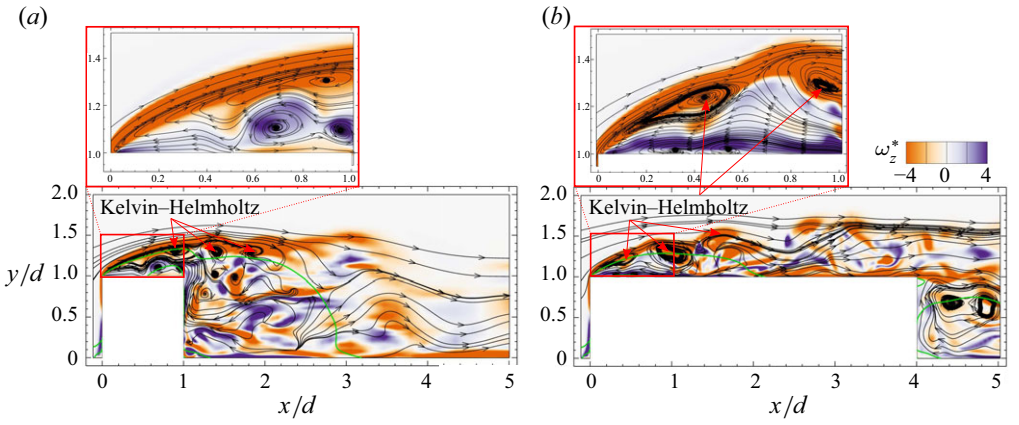

Figure 10. Contours of spanwise vorticity ω_z^* for (*a*) $DR = 1$ and (*b*) $DR = 4$, superimposed with instantaneous streamlines and the isopleth of $\overline{u} = 0$ (green line) at $z/d = 0$.

unsteady shear layer are less frequent and delayed, whereas they are more pronounced for $DR = 4$, and they occur more frequently, especially in the wake region ($1 \leqslant x/d \leqslant 6$). As such, it becomes apparent that large-scale vortex shedding is more pronounced for $DR = 4$ compared to $DR = 1$. Following the leading-edge shear layer separation and instability development, flapping-like motion (Cimarelli *et al.* 2018) leads to perturbations in the shear layer that amplify and propagate downstream, ultimately interacting with and influencing large-scale vortex shedding. Further evidence of shear layer flapping is presented in § 3.1, and discussion on interactions is presented in § 3.3.

Figure 10 present contours of spanwise vorticity (ω_z^*) for both prisms, superimposed with instantaneous streamlines and the isopleth of $\overline{u} = 0$ at $z/d = 0$. Formation of KHI rollers from the leading-edge shear layer is evident for both depth ratios. As presented in the insets, an early initiaion of KHI rollers is noted near the leading edge for $DR = 4$ compared to $DR = 1$, where the instability appears in the wake at $x/d \geqslant 1$. The onset of KHI rollers is quantified by the streamwise position of the first appearance of spanwise vortices, which is at $x/d \approx 0.4$ and 1 for $DR = 4$ and 1, respectively. This indicates that depth ratio significantly influences the onset of KHI rollers in the wake of a wall-mounted prism. Furthermore, the leading-edge shear layer sheds directly into the wake for the case $DR = 1$, while the flow reattaches on surfaces of the larger prism. The larger prism shows a prominent spanwise vortex shedding with hairpin-like vortices appearing over the prism surfaces. However, vortex shedding is suppressed by interactions between the separating shear layer and the wake in WR for the shorter prism. These observations, along with the formation of KHI rollers and their interaction with surfaces of the prism, are a precursor to the transition to turbulence in the wake of wall-mounted prisms.

Previous studies have noted that the wake dynamics is significantly influenced by the depth ratio and aspect ratio of the prism, as well as the flow Reynolds number (Wang *et al.* 2006; Rastan *et al.* 2021; Zargar *et al.* 2022; Goswami & Hemmati 2022). Rastan *et al.* (2021) showed that increasing depth ratio for a large-aspect-ratio prism resulted in decreased vortex shedding due to diminished interactions between the separating shear layer and the wake. This effect correlates with strengthening of the downwash flow. These results are consistent with the wake observed behind low-aspect-ratio prisms with changing depth ratio, where increasing depth ratio resulted in suppressed wake unsteadiness for $Re \leqslant 500$ (Goswami & Hemmati 2022). Further, Zargar *et al.* (2022) demonstrated that increasing the Reynolds number beyond 750 for a long prism ($DR = 5$)

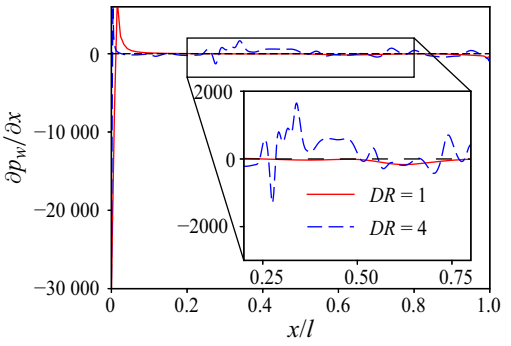

Figure 11. Axial wall pressure gradient ($\partial p_w/\partial x$) along the mid-span ($z/d = 0$) of both prisms at $Re = 2.5 \times 10^3$.

resulted in an irregular unsteady wake, resembling a transitional state. In summary, previous studies have indicated that increasing the depth ratio suppresses wake irregularity (Goswami & Hemmati 2022), while for a long prism, the wake evolves into an irregular unsteady wake with increasing Reynolds number (Zargar *et al.* 2022). This observation underscores the complexity of the flow dynamics around wall-mounted prisms, and suggests that multiple factors influence the interaction between the shear layer and wake structures, which results in wake transitions, such as the flow Reynolds number and prism geometry parameters. The present study portrays a novel perspective where the flow irregularity is enhanced with depth ratio. The current study focuses on the role of Reynolds number in the transition phenomenon, while investigating the influence of depth ratio on the wake dynamics. At moderate Reynolds numbers, the unsteadiness of the shear layer (Moore *et al.* 2019*a*) is stronger, interacting with the prism surfaces and elevating the flow momentum in this region due to large depth ratio. This further enhances the interactions between KHI and the wake coherent structures, leading to the wake transition. Evidence of this mechanism is discussed further in this paper by first presenting the unsteady shear layer motion, followed by the wake frequency signatures, and enhanced interactions using the Poisson equation. Finally, the triadic interactions are quantified using bi-spectral mode decomposition (BMD) to further understand the transition phenomenon. Here, we look at the interactions between KHI and the large-scale vortex shedding.

3.1. *Unsteady shear-layer motion*

We begin by first investigating the axial wall pressure gradient along the mid-span ($z/d = 0$) of both prisms at $Re = 2.5 \times 10^3$ in figure 11. The rapid increase in pressure gradient near the leading edge is attributed to streamwise flow compression due to an abrupt flow separation at the leading edge (Obabko & Cassel 2002). This yields a favourable pressure gradient, indicated by an overshoot of $\partial p_w/\partial x$ towards a positive value. Then the pressure gradient recovers for $DR = 1$ due to the absence of flow reattachment and shedding of the shea layer into the wake. For $DR = 4$, the pressure gradient remains elevated due to the reattachment of the shear layer on the prism surfaces. The elevated pressure gradients feature oscillatory motion, which results in flow compression and expansion (Obabko & Cassel 2002). This leads to an unsteady shear layer characterized by flapping-like motion. Similar oscillatory shear-layer motions are observed in infinite-span prisms (Kiya & Sasaki 1983; Cimarelli *et al.* 2018) as well as in two-dimensional forward–backward-facing steps (Fang & Tachie 2019). The unstable shear layer motion is associated with the formation

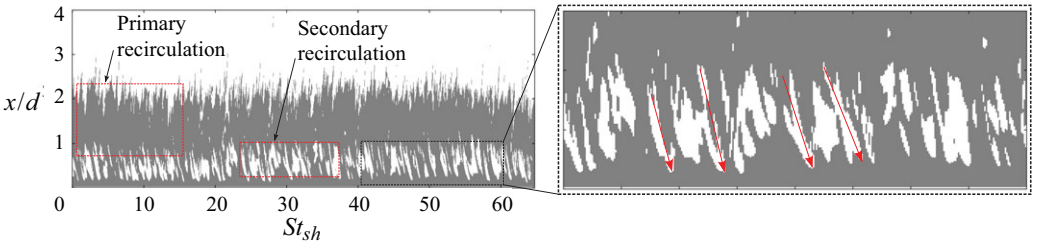

Figure 12. Space–time plot of the instantaneous wall shear stress (τ_w) along the top surface of the prism with $DR = 4$ at $z/d = 0$. Here, $\tau_w > 0$ (white) represents the region of forward flow, while $\tau_w < 0$ (grey) represents the region of reverse flow.

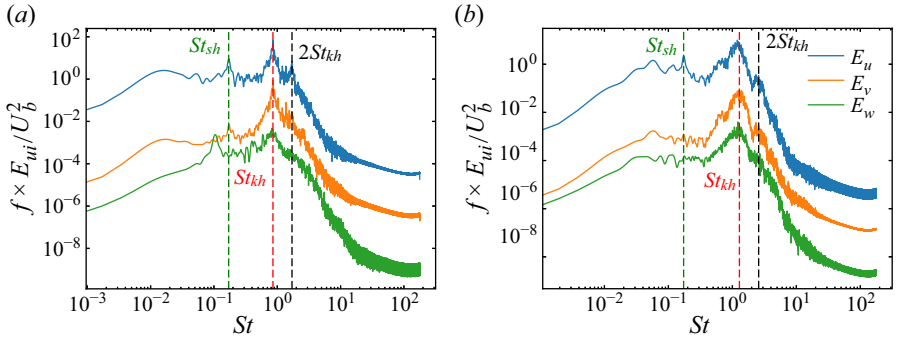

Figure 13. Pre-multiplied power spectral density of streamwise (E_u), normal (E_v) and spanwise (E_w) velocity fluctuations near the leading edge at (0.5, 1.3, 0) for (*a*) $DR = 1$ and (*b*) $DR = 4$.

of large-scale structures in the wake and their interactions, which are responsible for the momentum transport and mixing processes (More *et al.* 2015; Moore *et al.* 2019*a*).

Unsteady motion of the shear layer is analysed quantitatively using the wall shear stress ($\tau_w = \mu\ \partial u/\partial y$) along the top surface of the long prism, as depicted in figure 12. Temporal variations between the mean reattachment point are recognized by the border between the reverse flow ($\tau_w < 0$) and forward flow ($\tau_w > 0$) regions. Previous studies (Lander *et al.* 2018) suggest two main mechanisms that control the flow unsteadiness around sharp-edged prisms: vorticity roll-up and shear layer flapping. For long prisms, the shear layer roll-up near the leading edge intermittently forces the newly formed vortices towards the prism surfaces, resulting in a flapping motion (Moore *et al.* 2019*a*). This induces oscillations of the PR bubble between $x/d \approx 1.2$ and $x/d \approx 2.1$. As presented in figure 12, the mean reattachment point at $z/d = 0$ for the large-depth-ratio prism follows an oscillatory pattern. Further, SR also appears to oscillate, albeit in the opposite direction. With time, SR moves further upstream, while PR moves downstream. This behaviour may be linked to the mechanism of shear layer flapping, though it remains out of scope for this study, which focuses only on the transition phenomenon.

3.2. *Flow periodicity*

The flow periodicity is investigated by using the pre-multiplied power spectral density of the streamwise (E_u), normal (E_v) and spanwise (E_w) velocity fluctuations near the leading edge at (0.5, 1.3, 0) in figure 13. Multiple peaks are noted in the power spectrum

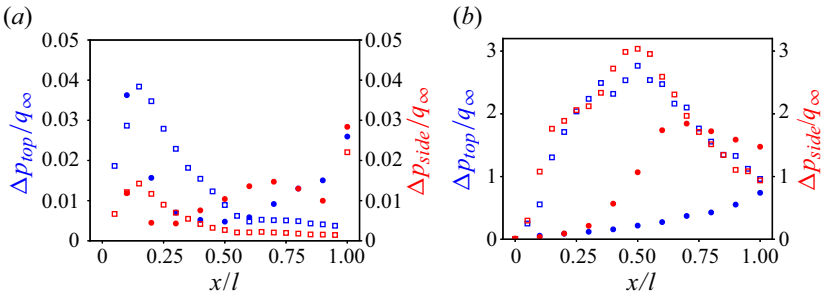

Figure 14. Profiles of maximum values of r.m.s. (*a*) turbulence–mean shear interaction (TMI_{max}) and (*b*) turbulence–turbulence interaction (TTI_{max}) terms of the Poisson equation for $DR = 1$ and 4 prisms at $z/d = 0$ (blue) and $y/d = 0.5$ (red). The axial distances are normalized using prism length (l). Circles represent $DR = 1$; squares represent $DR = 4$.

of both cases, with the one at St_{kh} appearing to be dominant. This frequency is associated with KHI of the leading-edge shear layer. Moreover, a harmonic of KHI is observed at $2St_{kh}$. Another frequency centred at St_{sh} is also observed, mainly attributed to the Kármán-like vortex shedding. At $DR = 1$, St_{sh} and St_{kh} are 0.170 and 0.855, respectively, while $St_{sh} = 0.173$ and $St_{kh} = 1.290$ at $DR = 4$. With increasing depth ratio from 1 to 4, a meagre increase in St_{sh} is noted, while St_{kh} and $2St_{kh}$ are significantly enhanced. In other words, the depth ratio enhances KHI of the leading-edge shear layer, and further explains the strong spanwise vortex shedding (observed in figure 8*b*). Additionally, as noted in figure 8(*a*), the formation of KHI rollers for $DR = 1$ occurs over a larger distance compared to $DR = 4$. This delay in the onset of KHI rollers is reflected in figure 13, where St_{kh} for $DR = 1$ is lower compared to $DR = 4$. This further suggests that structures associated with St_{kh} for $DR = 1$ are larger and slow-growing compared to $DR = 4$. Finally, a subharmonic spanwise frequency is noted, which is attributed to alternate shedding of the secondary vortex structures in the wake (Goswami & Hemmati 2022).

Motion of the unsteady shear layer is correlated with the vortex-pairing mechanism in sharp-edged prisms (Ma *et al.* 2023). Following the flow separation at the leading edge, both the shear layer rolls-up and newly formed vortices are intermittently forced towards the prism surfaces and convect downstream (flapping mechanism). These vortices pair with others in the wake, growing into large-scale structures, such as hairpin-like vortices (vortex-pairing mechanism). Large-scale vortex shedding away from the leading edge is associated with large-scale momentum transport. The vortex-pairing and interactions of KHI with large-scale vortices are quantified using the correlation $St_{kh}/St_{sh} = 0.18\,Re^{0.6}$ (Lander *et al.* 2018). Since these interactions are a function of Reynolds number, empirically this ratio should be $St_{kh}/St_{sh} = 18$ for $Re = 2.5 \times 10^3$ (Lander *et al.* 2018). For example, this ratio is $St_{kh}/St_{sh} = 26.5$ for flow around a two-dimensional square prism at $Re = 2 \times 10^3$ (Brun *et al.* 2008). In our cases, results in figure 13 indicate that this ratio is ~ 5.0 and ~ 7.5 for $DR = 1$ and 4, respectively. This suggests that interactions between KHI and large-scale structures depend on depth ratio, and they are suppressed compared to infinite-span and two-dimensional prisms (Brun *et al.* 2008; Kumahor & Tachie 2022), potentially due to the three-dimensional effects in the wake.

3.3. *Leading-edge shear layer interactions*

Interactions between KHI and large-scale vortex shedding can be further quantified by analysing the Poisson equation:

$$\nabla^2 p = -\rho \left(2 \overline{\frac{\partial u_i}{\partial x_j}} \frac{\partial u'_j}{\partial x_i} + \frac{\partial^2}{\partial x_i \, \partial x_j} (u'_i u'_j - \overline{u'_i u'_j}) \right). \tag{3.1}$$

Here, the right-hand side can be decomposed into two terms: turbulence–mean-shear interaction (TMI) and turbulence–turbulence interaction (TTI). The TMI accounts for the rapid changes in mean flow due to fluctuating fields, while TTI is associated with nonlinear interactions of turbulent structures. These two terms are considered the primary sources of pressure fluctuations in the flow (Ma *et al.* 2023). Figure 14 presents the profiles of maximum values of TMI and TTI terms of the Poisson equation for $DR = 1$ and 4 at $z/d = 0$ (blue) and $y/d = 0.5$ (red). Figure 14(*a*) reveals heightened TMI closer to the leading edge, where separated shear layers are created for both prisms. Following the abrupt shear layer separation at the leading edge, vorticity associated with the shear layer alters the mean flow in this region, resulting in enhanced momentum. This explains the high values of TMI near the leading edge. Initially, TMI_{max} for both prisms remains large, though it subsides quickly for $DR = 1$. Due to a lack of flow reattachment in $DR = 1$, TMI_{max} for the top shear layer reduces until $x/l \approx 0.5$, followed by a gradual increase due to flow interactions with the upwash flow at the trailing edge (Goswami & Hemmati 2023). The TMI for $DR = 4$ remains large in $0.1 \leqslant x/l \leqslant 0.3$, indicating a region of elevated mean flow modulations by KHI. For both cases, TMI_{max} on side surfaces is significantly suppressed compared to the top, indicating that the top surface shear layer plays a dominant role in driving the downstream flow. Finally, TMI points to the origins of mean flow modulations, which are associated with the shear layer flapping-like motion. Thus enhanced TMI near the leading edge for $DR = 4$ identifies the location where shear layer flapping-like motion is most pronounced.

The TTI term, presented in figure 14(*b*), highlights the interactions between different flow structures (Ma *et al.* 2023). While TMI is concentrated near the leading edge, TTI is more distributed across the top and side surfaces of both prisms. The distribution is likely due to the enhanced flow momentum (velocity fluctuations) produced by the mean flow alterations that gradually affect the surrounding flow field. For $DR = 1$, TTI_{max} is elevated closer to the trailing edge, which is attributed to direct shedding of the leading-edge shear layer into the wake. This enhances the interactions and vortex mixing in the wake region (Goswami & Hemmati 2023). For $DR = 4$, elevated TTI_{max} occurs close to the location of the flow reattachment on the prism surfaces ($\overline{x_R}/l \approx 0.53$). This region is associated with the breakdown of KHI rollers into hairpin-like vortices, which are then convected downstream. The interactions between KHI rollers and large-scale vortex shedding are most pronounced in this region, leading to an increased turbulence intensity and mixing (shown previously in figure 7*d*). These processes enhance the flow momentum due to an influx of energy by the mean flow modulation (TMI). As such, increased momentum results in the enhancement of vortex shedding and wake transition. These interactions are driven by the flow geometry, since such a mechanism is absent for the short prism, where TTI_{max} steadily rises up to the trailing edge. Finally, TTI_{max} is comparable for the top and side surface shear layers for both prisms, which indicates an invariance of energy production and dissipation on the top and side surfaces.

Triadic interactions form the basis of the energy transfer mechanism in the wake transition phenomenon (Craik 1971). The frequency triad, described by the interactions between two flow structures at frequencies St_i and St_j, results in a third frequency St_{i+j} such that $St_i \pm St_j \pm St_{i+j} = 0$. These interactions are quantified using BMD analysis, proposed by Schmidt (2020). Figure 15 shows the magnitude of the mode bi-spectrum for $DR = 4$ in the sum and difference regions. Their interactions with large-scale vortex shedding frequency (St_{sh}) are noted in figure 15 along with the sum interaction of St_{kh}

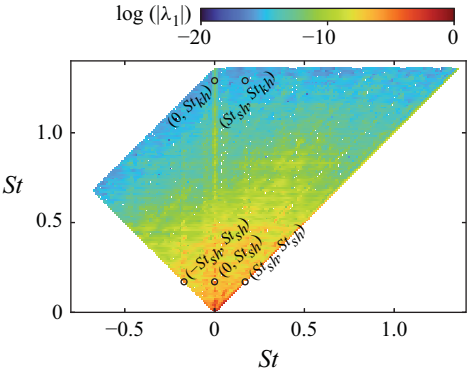

Figure 15. Magnitude mode bi-spectrum for $DR = 4$, using $N_{fft} = 2^{10}$, in the sum and difference regions.

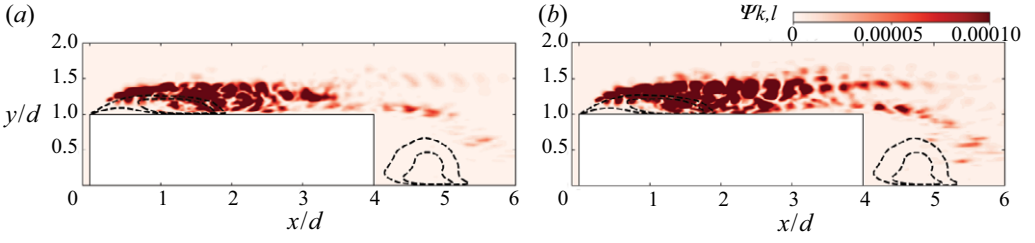

Figure 16. The BMD interaction map for the $DR = 4$ prism, showing the interactions between (a) KHI and mean flow, and (b) KHI and large-scale vortex shedding.

with St_{sh}, and the fundamental mode of St_{sh}. The intensity of the spectrum is large for the large-scale frequencies (St_{sh}), while it reduces significantly for St_{kh}. Further, the sum interaction of St_{sh} corresponds to the global maximum of the mode bi-spectrum, consistent with the separated flow in Schmidt (2020).

Interactions of KHI with the mean flow and large-scale vortex shedding are presented through a BMD interaction map in figure 16. This map quantifies the average local bi-correlation between the three frequencies, St_i, St_j and St_{i+j}, involved in the triad. The interactions are defined as $\Psi_{k,l} = |\phi_{k+l} \circ \phi_{k \circ l}|$, where ϕ_{k+l} represents the resultant mode of triadic interaction, and $\phi_{k \circ l}$ represents the influence of input modes. For more information regarding the formulation, readers are referred to Schmidt (2020). For both cases, the interactions are most pronounced near the leading edge and throughout the upper surface of the prism up to $x/d \approx 2$, where the flow reattaches to the surface. Interactions of KHI with the mean flow are dominant outside the PR, with the maximum value occurring at $x/d \approx 0.8$. This is consistent with the location of maximum TMI in figure 14(a). This interaction is associated with the mean flow modulation by KHI due to the shear layer flapping-like motion. A slightly elevated interaction at the trailing edge also corresponds to the trailing-edge shear layer interacting with the flow downstream. Interactions of KHI with large-scale vortex shedding are distributed across the prism surface. Near the centre of PR, these interactions enhance due to the flow impingement on prism surfaces as a result of the unsteady shear layer. This region of elevated interactions is consistent with the region of maximum TTI in figure 14(b). These results confirm that flow modulations at the leading edge, due to KHI, are convected downstream and interact with large-scale vortex shedding, enhancing the flow momentum. Due to the interactions and vortex breakdown, the flow momentum reduces further until the trailing edge. While not shown here for $DR =$

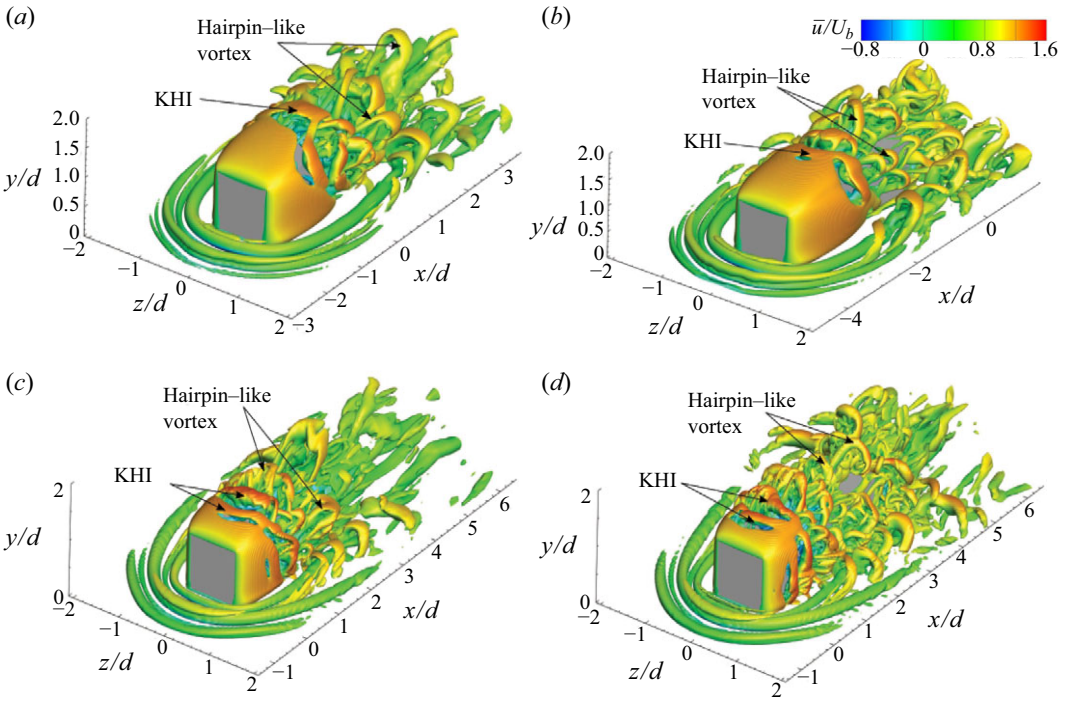

Figure 17. Instantaneous vortex structures overlaid with axial velocity (u) contours for (a,c) $DR = 1.5$ and (b,d) $DR = 3.5$ at (a,b) $Re = 1.5 \times 10^3$, (c,d) $Re = 4 \times 10^3$, identified using the Q-criterion ($Q^* = 1$).

1, such interactions remain absent, underscoring the influence of depth ratio in the wake transition phenomenon. These results provide a novel understanding of the interactions between KHI and large-scale vortex shedding in the wake of wall-mounted prisms.

3.4. *Observations across the parameter space*

Observations and insights from the specific cases $DR = 1$ and 4 at $Re = 2.5 \times 10^3$ are expandable across the broad parameter space considered in this study, i.e. varying aspect ratio (0.25−1.5), depth ratio (1−4) and Reynolds numbers (1×10^3−5×10^3). For example, we consider the cases $DR = 1.5$ and 3.5 at $Re = 1.5 \times 10^3$ and 4×10^3 in figure 17. These instantaneous vortex structures reveal that for a short-depth-ratio prism ($DR = 1.5$), the leading-edge shear layer extends and sheds directly into the wake. The influence of the Reynolds number becomes apparent, where the unsteady wake is classified into regular unsteady wake, consistent with the observations of Zargar *et al.* (2022). In contrast, a larger-depth-ratio prism ($DR = 3.5$) exhibits the shear layer reattachment to the prism surfaces, leading to an unsteady shear layer motion and enhanced interactions with large-scale vortex shedding. This results in the formation of large-scale vortex rollers and hairpin-like vortices in the wake, consistent with previous observations from the case $DR = 4$ at $Re = 2.5 \times 10^3$.

Next, we consider the cases of prisms with $AR = 1.5$ and $DR = 1.5, 3.5$ at $Re = 2.5 \times 10^3$ in figure 18. The results are consistent with the observations from $AR = 1$, where the interactions of KHI with large-scale vortex shedding is more pronounced for larger depth ratio. This results in a more complex wake topology downstream of the leading edge, as opposed to $DR = 1.5$, where shedding of the shear layer into the wake suppresses the interactions, resulting in a more stable flow. Influence of prism aspect

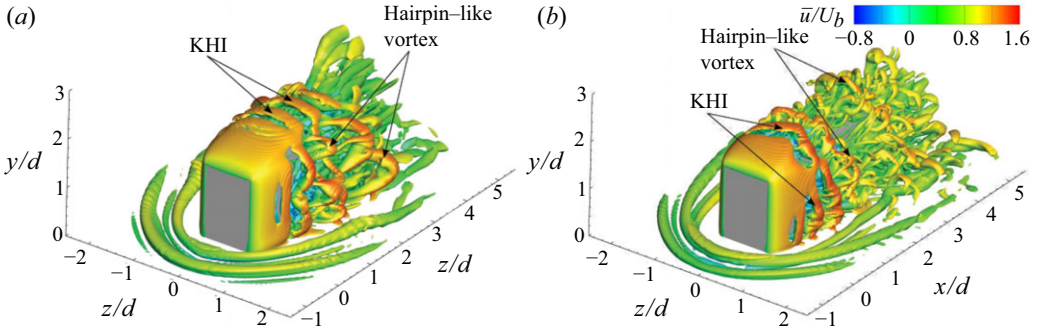

Figure 18. Instantaneous vortex structures overlaid with axial velocity (u) contours for prisms with $AR = 1.5$ and (a) $DR = 1.5$ and (b) $DR = 3.5$ at $Re = 2.5 \times 10^3$ identified using the Q-criterion ($Q^* = 1$).

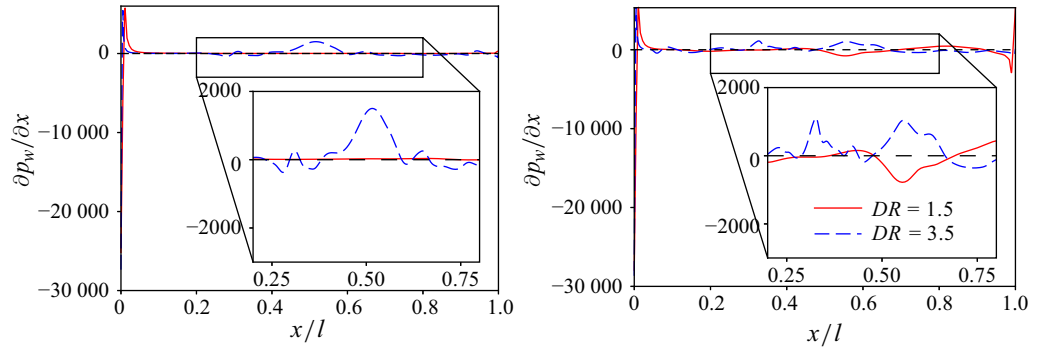

Figure 19. Axial wall pressure gradient along the mid-span ($z/d = 0$) of prisms with (a) $AR = 1.5$ at $Re = 2.5 \times 10^3$, and (b) $AR = 1$ at $Re = 4 \times 10^3$.

ratio is further evident in figure 18, where the flow unsteadiness enhances with aspect ratio, consistent with observations of Saha (2013). Finally, the unsteady shear layer is quantitatively observed by axial wall pressure gradients plotted along the prism mid-span ($z/d = 0$) in figure 19. Here, we present the cases $DR = 1.5$, 3.5 with $AR = 1.5$ at $Re = 2.5 \times 10^3$, and $AR = 1$ at $Re = 4 \times 10^3$. The rapid overshoot of pressure gradient near the leading edge, suggesting an abrupt flow separation, is consistent in all cases. The trends of $\partial p_w/\partial x$ for $DR = 1.5$ remain steady at $Re = 2.5 \times 10^3$, while small oscillations are noted at $Re = 4 \times 10^3$. Although Reynolds number effects are not the primary focus of this study, the oscillations in $\partial p_w/\partial x$ at higher Reynolds numbers can be linked to unsteady wake dynamics. Notably, for a larger-depth-ratio prism ($DR = 3.5$), the oscillatory behaviour of the pressure gradient becomes evident and more pronounced across both aspect ratios and Reynolds numbers. Oscillations enhance with depth ratio, and they are associated with the shear layer flapping-like phenomenon, which is pronounced for these cases (see figures 17 and 18). Previous studies (Goswami & Hemmati 2022, 2023) have established that unsteady and mean wake topology of wall-mounted prisms are functions of both Reynolds number and body geometry. Our results expand this argument to turbulence transition, where the interactions between KHI and large-scale vortex shedding are enhanced with increasing depth ratio. These interactions are driven by the unsteady shear layer motion, which is most pronounced for large-depth-ratio prisms. These interactions enhance the flow momentum over the prism surfaces, resulting in a more complex wake structure, and ultimately leading to turbulence transition.

4. Conclusion

This study numerically investigated the wake transition phenomenon around wall-mounted prisms. Results were presented at Reynolds number 2.5×10^3 for prisms with aspect ratio 1 and depth ratios 1 and 4, which were consistent for the entire parameter space studied here ($AR = 0.25{-}1.5$, $DR = 1{-}4$ and $Re = 1 \times 10^3{-}5 \times 10^3$). The wake unsteadiness is enhanced with increasing depth ratio. Kelvin–Helmholtz instability (KHI) is noted for all cases, forming finite spanwise vortex rollers. However, the intensity and frequency of the rollers are more pronounced for longer prisms ($DR \geqslant 3$), while for short prisms they are delayed and less frequent. Additionally, the formation of KHI for short prisms takes place over a larger distance compared to longer prisms. Enhanced wake unsteadiness is attributed to interactions between KHI and large-scale vortex shedding, induced by an unsteady shear layer flapping-like motion in the wake of large-depth-ratio prisms. Evidence of an unsteady shear layer is provided by analysing the space–time wall shear stress contours, showing an oscillating recirculating region. Interactions between KHI and large-scale vortex shedding are quantified using the Poisson equation and bi-spectral decomposition. The turbulence–mean-shear interaction (TMI) term of the Poisson equation is elevated near the leading edge, while the turbulence–turbulence interaction (TTI) term is distributed across the prism surfaces. Elevated TMI near the leading edge points to the mean flow manipulations due to the unsteady shear layer, while enhanced TTI on the prism surfaces indicates interactions between KHI and large-scale vortex shedding. Elevated TMI shows that the leading-edge flow manipulations provide energy, which is then transferred to the large-scale vortex shedding, enhancing the flow momentum. Increased momentum in the wake enhances vortex shedding, which is a precursor to turbulence transition. Finally, bi-spectral mode decomposition analysis provides evidence of the interactions between KHI and large-scale vortex shedding, further confirming the transition process. This study underscores the role of depth ratio in the transition to turbulence phenomenon at moderate Reynolds numbers, and provides novel insights into the interaction mechanisms of KHI and large-scale vortex shedding in the wake of wall-mounted prisms.

Acknowledgements. This research has received support from the Natural Sciences and Engineering Research Council of Canada (NSERC) and Alberta Innovates. The computational analysis was completed using Digital Research Alliance of Canada computing clusters.

Declaration of interests. The authors report no conflict of interest.

References

BEHERA, S. & SAHA, A.K. 2019 Characteristics of the flow past a wall-mounted finite-length square cylinder at low Reynolds number with varying boundary layer thickness. *J. Fluids Engng* **141** (6), 061204.

BOURGEOIS, J.A., SATTARI, P. & MARTINUZZI, R.J. 2011 Alternating half-loop shedding in the turbulent wake of a finite surface-mounted square cylinder with a thin boundary layer. *Phys. Fluids* **23** (9), 095101.

BRUN, C., AUBRUN, S., GOOSSENS, T. & RAVIER, P. 2008 Coherent structures and their frequency signature in the separated shear layer on the sides of a square cylinder. *Flow Turbul. Combust.* **81** (1–2), 97–114.

CELIK, I., KLEIN, M. & JANICKA, J. 2009 Assessment measures for engineering LES applications. *J. Fluids Engng* **131** (3), 031102.

CIMARELLI, A., LEONFORTE, A. & ANGELI, D. 2018 On the structure of the self-sustaining cycle in separating and reattaching flows. *J. Fluid Mech.* **857**, 907–936.

CRAIK, A.D.D. 1971 Non-linear resonant instability in boundary layers. *J. Fluid Mech.* **50** (2), 393–413.

DURBIN, P.A. & REIF, B.A.P. 2011 *Statistical Theory and Modeling for Turbulent Flows*. John Wiley & Sons.

FANG, X. & TACHIE, M.F. 2019 Flows over surface-mounted bluff bodies with different spanwise widths submerged in a deep turbulent boundary layer. *J. Fluid Mech.* **877**, 717–758.

GOSWAMI, S. & HEMMATI, A. 2020 Response of turbulent pipeflow to multiple square bar roughness elements at high Reynolds number. *Phys. Fluids* **32** (7), 075110.

GOSWAMI, S. & HEMMATI, A. 2021*a* Evolution of turbulent pipe flow recovery over a square bar roughness element at a range of Reynolds numbers. *Phys. Fluids* **33** (3), 035113.
GOSWAMI, S. & HEMMATI, A. 2021*b* Response of viscoelastic turbulent pipeflow past square bar roughness: the effect on mean flow. *Computation* **9** (8), 85.
GOSWAMI, S. & HEMMATI, A. 2022 Mechanisms of wake asymmetry and secondary structures behind low aspect-ratio wall-mounted prisms. *J. Fluid Mech.* **950**, A31.
GOSWAMI, S. & HEMMATI, A. 2023 Mean wake evolution behind low aspect-ratio wall-mounted finite prisms. *Intl J. Heat Fluid Flow* **104**, 109237.
GOSWAMI, S. & HEMMATI, A. 2024 Impact of depth-ratio on shear-layer dynamics and wake interactions around wall-mounted prisms. *Phys. Fluids* **36** (11), 115149.
HEMMATI, A., WOOD, D.H. & MARTINUZZI, R.J. 2016 Effect of side-edge vortices and secondary induced flow on the wake of normal thin flat plates. *Intl J. Heat Fluid Flow* **61**, 197–212.
HEMMATI, A., WOOD, D.H. & MARTINUZZI, R.J. 2018 On simulating the flow past a normal thin flat plate. *J. Wind Engng Ind. Aerodyn.* **174**, 170–187.
KIYA, M. & SASAKI, K. 1983 Structure of a turbulent separation bubble. *J. Fluid Mech.* **137**, 83–113.
KUMAHOR, S. & TACHIE, M.F. 2022 Turbulent flow around rectangular cylinders with different streamwise aspect ratios. *J. Fluids Engng* **144** (5), 051304.
LANDER, D.C., MOORE, D.M., LETCHFORD, C.W. & AMITAY, M. 2018 Scaling of square-prism shear layers. *J. Fluid Mech.* **849**, 1096–1119.
MA, C.H., AWASTHI, M., MOREAU, D. & DOOLAN, C. 2023 Aeroacoustics of turbulent flow over a forward–backward facing step. *J. Sound Vib.* **563**, 117840.
MARTINUZZI, R.J. 2008 Dual vortex structure shedding from low aspect ratio, surface-mounted pyramids. *J. Turbul.* **9**, N28.
MOIN, P. & MAHESH, K. 1998 Direct numerical simulation: a tool in turbulence research. *Annu. Rev. Fluid Mech.* **30** (1), 539–578.
MOORE, D.M., LETCHFORD, C.W. & AMITAY, M. 2019*a* Energetic scales in a bluff body shear layer. *J. Fluid Mech.* **875**, 543–575.
MOORE, D.M., LETCHFORD, C.W. & AMITAY, M. 2019*b* Transitional shear layers on rectangular sections. In Proceedings of the XV Conference of the Italian Association for Wind Engineering: IN-VENTO, vol. **25**, pp. 519–533. Springer.
MORE, B.S., DUTTA, S., CHAUHAN, M.K. & GANDHI, B.K. 2015 Experimental investigation of flow field behind two tandem square cylinders with oscillating upstream cylinder. *Exp. Therm. Fluid Sci.* **68**, 339–358.
OBABKO, A.V. & CASSEL, K.W. 2002 Navier–Stokes solutions of unsteady separation induced by a vortex. *J. Fluid Mech.* **465**, 99–130.
POPE, S.B. 2001 Turbulent flows. *Meas. Sci. Technol.*, **12** (11), 2020–2021.
RASTAN, M.R., SHAHBAZI, H., SOHANKAR, A., ALAM, M.M. & ZHOU, Y. 2021 The wake of a wall-mounted rectangular cylinder: cross-sectional aspect ratio effect. *J. Wind Engng Ind. Aerodyn.* **213**, 104615.
SAEEDI, M., LEPOUDRE, P.P. & WANG, B.C. 2014 Direct numerical simulation of turbulent wake behind a surface-mounted square cylinder. *J. Fluids Struct.* **51**, 20–39.
SAHA, A.K. 2013 Unsteady flow past a finite square cylinder mounted on a wall at low Reynolds number. *Comput. Fluids* **88**, 599–615.
SCHMIDT, O.T. 2020 Bispectral mode decomposition of nonlinear flows. *Nonlinear Dyn.* **102** (4), 2479–2501.
SOHANKAR, A., NORBERG, C. & DAVIDSON, L. 1998 Low-Reynolds-number flow around a square cylinder at incidence: study of blockage, onset of vortex shedding and outlet boundary condition. *Intl J. Numer. Meth. Fluids* **26** (1), 39–56.
WANG, H.F. & ZHOU, Y. 2009 The finite-length square cylinder near wake. *J. Fluid Mech.* **638**, 453–490.
WANG, H.F., ZHOU, Y., CHAN, C.K. & LAM, K.S. 2006 Effect of initial conditions on interaction between a boundary layer and a wall-mounted finite-length-cylinder wake. *Phys. Fluids* **18** (6), 065106.
YAKHOT, A., LIU, H. & NIKITIN, N. 2006 Turbulent flow around a wall-mounted cube: a direct numerical simulation. *Intl J. Heat Fluid Flow* **27** (6), 994–1009.
ZARGAR, A., TAROKH, A. & HEMMATI, A. 2022 The unsteady wake transition behind a wall-mounted large-depth-ratio prism. *J. Fluid Mech.* **952**, A12.
ZDRAVKOVICH, M.M. 1997 *Flow around circular cylinders*, Vol. **1**.: *Fundamentals*. Oxford Science Publications.
ZHANG, Z., KAREEM, A., XU, F. & JIANG, H. 2023 Global instability and mode selection in flow fields around rectangular prisms. *J. Fluid Mech.* **955**, A19.